M. Aronniemi, J. Sainio, J. Lahtinen, Characterization and gas-sensing behavior of an iron oxide thin film prepared by atomic layer deposition, Helsinki University of Technology, Publications in Engineering Physics A, Report TKK-F-A850 (2007).

© 2007 by authors

Characterization and gas-sensing behavior of an iron oxide thin film prepared by atomic layer deposition

M. Aronniemi *, J. Sainio J. Lahtinen

Laboratory of Physics, Helsinki University of Technology, P.O.Box 1100, FI-02015 TKK, Finland

Abstract

In this work we investigate an iron oxide thin film grown with atomic layer deposition (ALD) for a gas sensor application. The objective is to characterize the structural, chemical, and electrical properties of the film, and to demonstrate its gas-sensitivity. The obtained SEM and AFM results indicate that the film has a granular structure and that it has grown mainly on the glass substrate leaving the platinum electrodes uncovered. XRD results show that iron oxide is in the α-Fe_2O_3 (hematite) phase. XPS spectra recorded at elevated temperature imply that the surface iron is mainly in the Fe^{3+} state and that oxygen has two chemical states: one corresponding to the lattice oxygen and the other to adsorbed oxygen species. Electric conductivity has an activation energy of 0.3–0.5 eV and almost Ohmic I–V dependency. When exposed to O_2 and CO, a typical n-type response is observed.

Key words: iron oxide, thin film, gas sensor, atomic layer deposition
PACS:

1 Introduction

Semiconductive metal oxides are widely studied in order to develop inexpensive and simple gas sensors. Their applications are typically in monitoring combustible or toxic gases, such as O_2, CO, H_2, NO_2, and CH_4. Metal oxide functions as a gas-sensitive material by changing its resistance due to exposure to oxidizing or reducing gases. Typically, the target gas affects the sensor

* Corresponding author.
Email address: Mikko.Aronniemi@tkk.fi (M. Aronniemi).

resistance by changing the density of adsorbed oxygen and/or by changing the concentration of oxygen vacancies in the lattice [1].

The gas-sensitive material can be incorporated in the sensor as a thick film, thin film, or compressed, and possibly sintered, powder. The advantage of using a thin film is that it makes the sensor fabrication compatible with IC manufacturing processes, thus allowing miniaturization and low production costs. In addition, a thin sensing layer results typically in high sensitivity, rapid response, and low power consumption.

Besides the most popular gas-sensitive oxides, e.g. SnO_2 and ZnO_2, iron oxides, either pure or doped, have been investigated for sensor applications by several authors, and promising results have been obtained [2–19]. Iron oxide thin film gas sensors have been prepared by, e.g., RF sputtering [5], evaporation [6], chemical vapor deposition [7,8], sol–gel processing [11,12,15], spray pyrolysis [13], and liquid-phase deposition [17].

In this work, we investigate an iron oxide thin film grown with atomic layer deposition (ALD) for a gas sensor application. In particular, we characterize the structural, chemical, and electrical properties of the film, and demonstrate its sensitivity to O_2 and CO taken as examples of an oxidizing and reducing target gas, respectively. In ALD the film is grown in sequential cycles consisting of self-terminating gas–solid reaction steps. This provides a straightforward thickness control and typically produces highly uniform and conformal films [20–22], allowing also convenient doping [23]. Previously, the growth of Fe_2O_3 thin films with ALD has been reported by de Ridder et al. [24], Lim et. al [25], and Lie et al. [26]. Regarding gas sensor applications, the use of ALD-grown SnO_2 thin film has been reported by Utriainen et al. [27] and Rosental et al. [28].

2 Experimental

The sensor sample was prepared on a 4×4 mm^2 glass substrate. Before the film deposition, platinum electrodes for resistance measurement and temperature control were evaporated on the top and bottom side of the substrate, respectively. The electrode structure for resistance measurement consisted of 22 pairs of interdigital electrodes having a width of 20 μm, length of $\sim$ 2 mm, and spacing of 20 μm. The iron oxide film was grown with 5000 ALD cycles at 500 °C using $FeCl_3$ and H_2O as precursors; this metal precursor is different than previously reported for the ALD growth of iron oxide [24–26]. A high deposition temperature was chosen to avoid chlorine remnants and to ensure thermal stability of the oxide.

The crystal structure of iron oxide was characterized with XRD (x-ray diffraction) using a Philips PW1830 spectrometer with Cu Kα radiation (8.04 keV). The film morphology was investigated with AFM (atomic force microscopy) and field-emission SEM (scanning electron microscopy). The AFM images were recorded with a Digital Instruments Nanoscope III operated in ambient conditions in the dynamic mode with amplitude modulation. The SEM imaging was performed with a LEO DSM-982 Gemini microscope.

For the chemical analysis of the sensor surface, XPS (x-ray photoelectron spectroscopy) was utilized. The measurements were conducted with a Surface Science Instruments SSX-100 ESCA spectrometer using monochromatic Al K_α x-rays (1486.6 eV) and an electrostatic hemispherical analyzer. The spectra were recorded with a pass energy of 55 eV and an x-ray spot size of 600 μm, which gave for the Au $4f_{7/2}$ peak a FWHM of 0.95 eV. The binding energy step size was 0.05 eV or 0.1 eV. The base pressure in the chamber was around 10^{-9} mbar.

Measuring the sensor resistance and controlling its temperature were accomplished with National Instruments Field Point modules and a LabVIEW-based user interface including a PID control for the sensor temperature. The sampling period was 1.5 s. The bias voltage source was connected to provide a constant voltage of 2.0 V over the sensor, irrespective of the sensor resistance.

For gas exposure experiments, the sensor sample was mounted in a stainless steel chamber which was pumped with a turbomolecular pump; the base pressure was 10^{-7} mbar. Using a vacuum chamber allowed well-defined gas exposures in a wide pressure range of 10^{-7}–10^{-2} mbar. Manual leak valves were used for gas dosing and the pressure was measured with Pirani and cold cathode gauges (Pfeiffer PKR 251). Gases used in the exposures were O_2 (99.999 %) and CO (99.997 %) (AGA).

3 Results and discussion

3.1 Characterization

Figure 1 shows SEM images of the iron oxide film and an edge of a platinum electrode. AFM images of the film are presented in Fig. 2 and a typical section line in Fig. 3. It is observed that the film consists of various shapes of agglomerates whose lateral diameter varies typically between 100 and 400 nm and height between 50 and 200 nm. Although films grown with ALD are usually uniform and conformal, formation of oxide particles, e.g. ZrO_2 and TiO_2, has been reported when using chloride reactants with oxide substrates

[29–31]. Increasing the growth temperature has been observed to enhance the particle formation [29–32]. While undesired for typical ALD applications, e.g. microelectronic devices, granular film structure is generally advantageous in gas sensors due to increased surface area which improves the sensitivity.

Figures 1 and 3 indicate also that the film has grown mainly on the glass substrate leaving the platinum electrodes mostly uncovered; only separate grains of iron oxide could be detected on the electrodes (not shown). The absence of iron oxide on the electrodes was confirmed with XPS by monitoring the Fe 2p intensity while moving the x-ray spot (150 μm) from the substrate onto the electrode. In ALD with a chloride precursor and oxide substrate, the chloride precursor is considered to react primarily with surface -OH groups [31]. Thus, the observed selective growth could be attributed to the obvious difference in the density of -OH groups between the SiO_2 substrate and the platinum electrode. The catalytic nature of typical electrode materials, e.g. platinum, may affect the sensor response [33]. Therefore, the ability to deposit the metal oxide film so that the electrodes are left uncovered may be useful for optimizing the sensor performance.

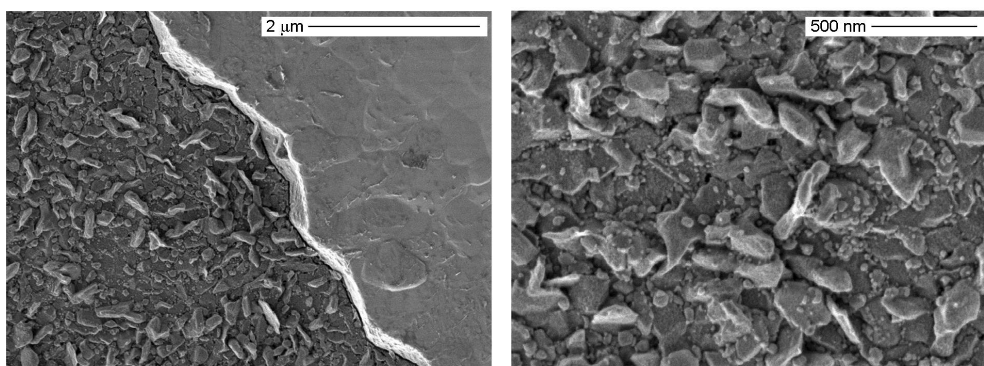

Fig. 1. SEM micrographs of the sensor surface. An edge of a platinum electrode is seen in the left-hand image.

XRD pattern of the iron oxide film, recorded from a sample without the electrodes, is shown in Fig. 4. All the observed diffraction maxima correspond to the α-Fe_2O_3 phase (hematite). Our earlier study showed that the phase can be controlled with the deposition temperature: growing the film at 350 °C resulted in the γ-Fe_2O_3 (maghemite) phase whereas the α-Fe_2O_3 (hematite) phase was obtained at 400 °C or above [32]. Interestingly, both of these phases can be used as a gas-sensitive material: On one hand, γ-Fe_2O_3 and Fe_3O_4 form a reversible reduction–oxidation pair due to their similar crystal structures, and these phases differ in conductivity by several decades [3]. Thus, gas-sensitivity is obtained through the gas-induced changes in the stoichiometry of the oxide. On the other hand, α-Fe_2O_3 is a thermally stabile n-type semiconductor where the conductivity results from oxygen vacancies [16,34,35]; the reported band gap values are between 2.0 and 2.7 eV [36,37]. Oxides of this type, e.g.

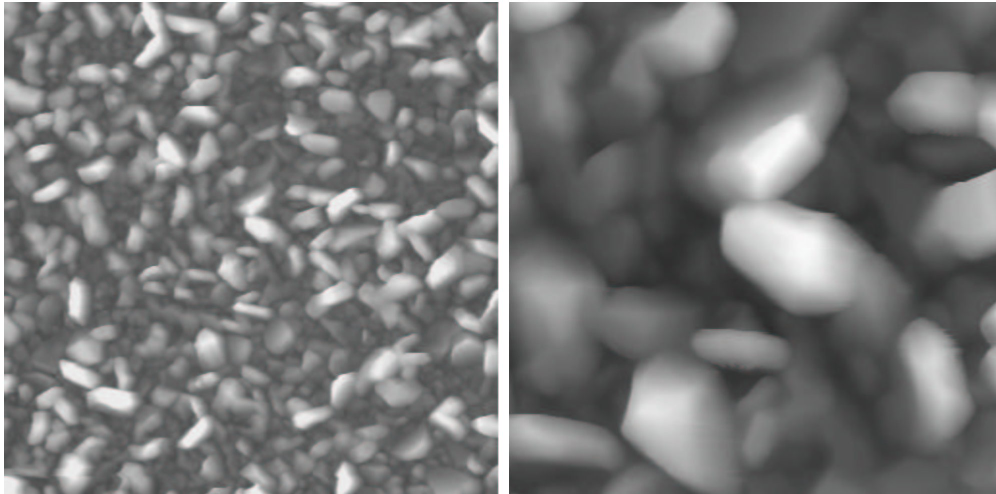

Fig. 2. AFM images of the film surface. The image sizes are 4×4 μm^2 (left) and 1×1 μm^2 (right).

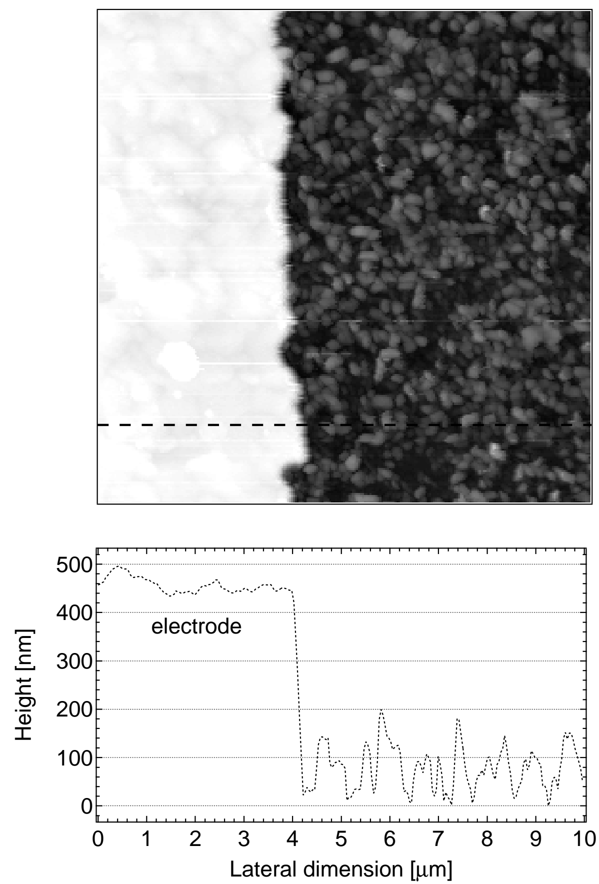

Fig. 3. A typical AFM section across the electrode edge (bottom) and the corresponding AFM image (10×10 μm^2) with the section indicated with a dashed line (top).

SnO_2, exhibit gas-sensitivity based on the effect of adsorbed oxygen [1]. In the following, the discussion is limited to the α-Fe_2O_3 phase.

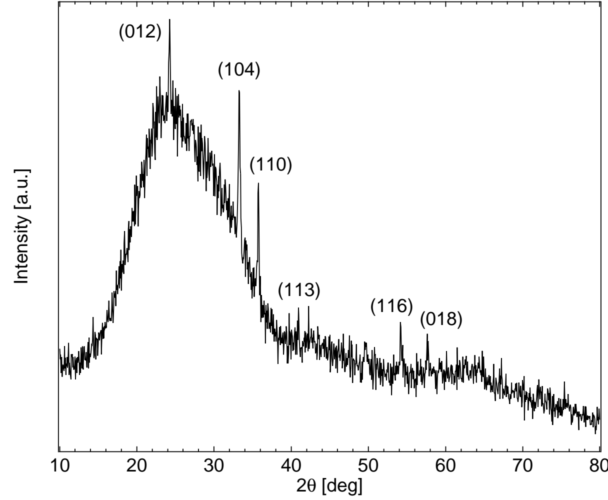

Fig. 4. XRD pattern of the iron oxide film. The diffraction maxima have been identified according to Ref. [38] and they indicate the α-Fe_2O_3 phase (hematite).

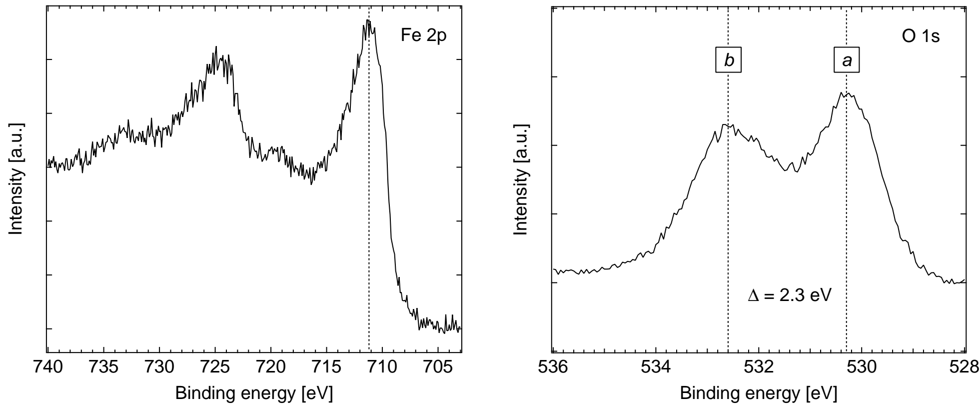

Fig. 5. Fe 2p and O 1s photoemission spectra recorded at 400 °C. The O 1s components can be explained as a = lattice O^{2-} and b = adsorbed oxygen.

Figure 5 shows the Fe 2p and O 1s photoelectron spectra of the iron oxide film; the x-ray spot area (600 μm) contained both substrate and electrode surface. During the spectrum acquisition, the sensor temperature was set to 400 °C to ensure high conductivity of the film (to avoid differential charging) and to be in a realistic operating temperature. The maximum of the Fe $2p_{3/2}$ peak is at 711.2 eV and the satellite peak between the $2p_{3/2}$ and $2p_{1/2}$ peaks is clearly visible. Comparing these observations as well as the overall shape of the spectrum with those reported in literature, e.g. in Refs. [32,39–41], it can be concluded that iron is mainly in the Fe^{3+} state. This is in accordance with the XRD results because Fe_2O_3 contains only Fe^{3+} ions. However, when the x-ray spot was moved far from the electrodes (not shown), the Fe^{3+} features

became even more prominent. This suggests that the presence of the platinum electrodes has a slight reducing effect on iron.

The O 1s spectrum (Fig. 5) shows two components with a binding energy separation of $\sim$ 2.3 eV. The lower binding energy component a at 530.3 eV can be assigned to O^{2-} in the iron oxide lattice. According to literature, the higher binding energy component b could be explained with adsorbed oxygen species such as $O_2{}^{2-}$ [41–43]. This is supported by an observation that when the sample was sputtered slightly with 4-keV argon ions, the intensity of component b decreased significantly with respect to component a. Another explanation for component b could be OH^- originating from the H_2O precursor used in the growth process.

The survey spectrum (not shown) had strong platinum peaks supporting the SEM and AFM observation that the electrodes are mostly uncovered of iron oxide. The maximum of the Pt $4f_{7/2}$ peak was located at 71.3 eV, which implies the metallic state. Chlorine from the iron precursor was not observed. Carbon contamination, probably due to atmospheric exposure, disappeared when the sensor temperature was increased above the room temperature.

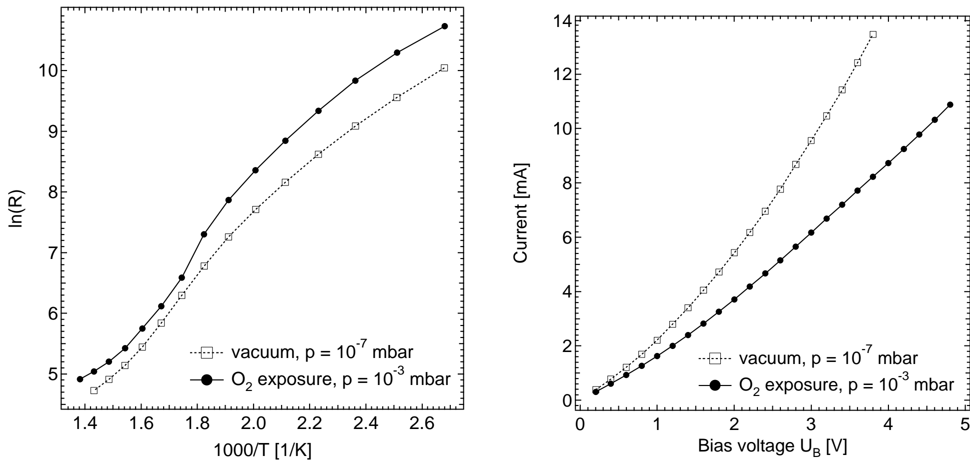

Fig. 6. Arrhenius curves with $U_B = 2.0$ V (left) and I–V curves at 300 °C (right) corresponding to two pressures. The curve connecting the data points is only to guide the eye.

Figure 6 shows Arrhenius curves ($\ln(R)$ vs. $1/T$) and I–V curves of the iron oxide film. These were recorded both in a vacuum of 10^{-7} mbar and under oxygen exposure of 10^{-3} mbar. The Arrhenius curves are not completely linear in the studied temperature range (100–425 °C) but a straight-line fit gives an activation energy of 0.3–0.5 eV, depending on the points included in the fit. Several sources could contribute to the activation energy: ionization of donors, hopping of conduction electrons between polaron states, a Schottky barrier at the electrode–semiconductor contact, and a barrier at grain boundaries caused by band bending due to localized surface states. However, the Arrhenius plots

indicate that although the oxygen exposure decreases the resistance, it does not affect the activation energy. Thus, it seems likely that the sensor response, described below, is not based on changes in the height of the Schottky barrier or the grain boundary barriers. The I–V curves (Fig. 6) show that the sensor behavior is close to Ohmic. The slight upward curvature could be ascribed to, e.g., a Schottky barrier at the electrode contact.

3.2 Gas-sensing behavior

In order to characterize the gas-sensing behavior of the film, the chamber was first evacuated to 1×10^{-7} mbar and then the sensor was subjected to a gas exposure sequence consisting of 30-min steps described in Table 1.

The gas exposures were performed at 200 °C, 300 °C, and 400 °C, and the resulting dynamic responses are plotted in Fig. 7. Due to the strong temperature dependency, the resistance values have been normalized with the initial resistance of the sensor in vacuum.

The sensing behavior seems to be qualitatively similar in the three studied temperatures and is typical for n-type oxides. The resistance started to increase rapidly when O_2 was introduced into the chamber (step a), and when the exposure was stopped, the resistance started to decrease (b). According to the commonly used model for the sensing mechanism of n-type oxides, see e.g. Ref. [1], the adsorbing oxygen generates localized surface states which trap conduction band electrons; this leads to increase in the resistance. Another possibility is that the adsorbing oxygen enters into the lattice and fills there oxygen vacancies. This mechanism, too, decreases the density of conduction electrons leading to increase in the resistance. Step b in the dynamic response (Fig. 7) shows that when the O_2 exposure was stopped, the surface started to get restored.

The effect of CO is observed to depend on the preceding gas exposure: following an O_2 exposure CO made the resistance decrease rapidly (d), whereas after a vacuum period (e) its effect was negligible (f). The O_2 response of the CO-exposed sensor (g) is almost similar to that of an un-exposed sensor (a). This suggests that CO removed the adsorbed oxygen rapidly (d), the surface became clean (e), and CO was not adsorbed on the clean surface (f). These observations indicate that the sensing of CO occurs mainly via a reaction with the adsorbed oxygen.

When CO was added to the O_2 exposure (with an equal partial pressure), the resistance decreased sharply (h). This decrease was, however, not as large as in the pure CO exposure (d), and the resistance almost stabilized. Finally, stopping the CO exposure caused the sensor to continue the preceding O_2

Table 1
Steps of the gas exposure sequence corresponding to Fig. 7. Duration of each step was 30 min.

Step	Gas	Pressure (mbar)
initial	vacuum	$\sim 10^{-7}$ mbar
a	O_2	1×10^{-3} mbar
b	vacuum	$\sim 10^{-7}$ mbar
c	O_2	1×10^{-3} mbar
d	CO	1×10^{-3} mbar
e	vacuum	$\sim 10^{-7}$ mbar
f	CO	1×10^{-3} mbar
g	O_2	1×10^{-3} mbar
h	O_2+CO	2×10^{-3} mbar
i	O_2	1×10^{-3} mbar

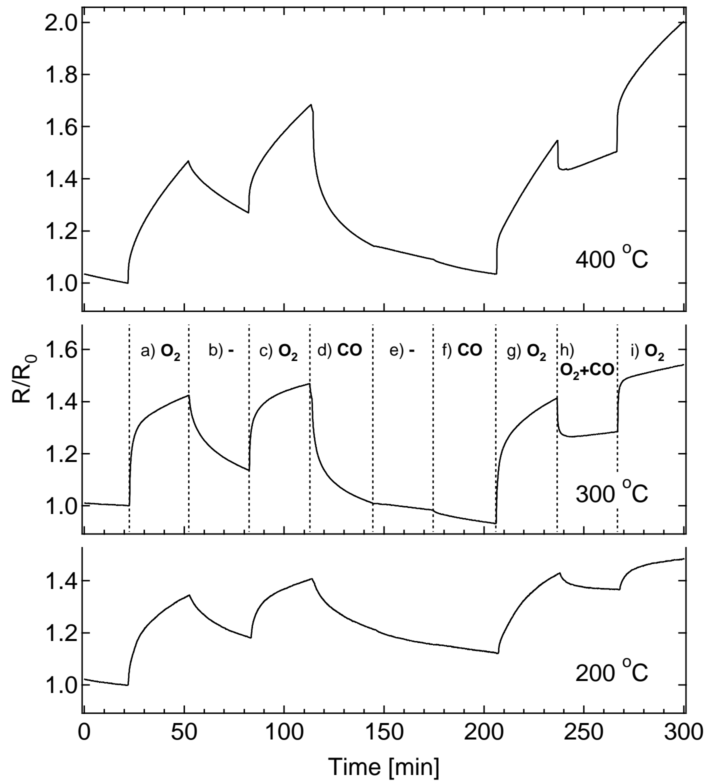

Fig. 7. Dynamic response to successive O_2 and CO exposures recorded at 200 °C 300 °C, and 400 °C. The exposure steps are described in Table 1.

response (i). The observed behavior seems to reflect two competing reactions: oxygen adsorption and CO removing the adsorbed oxygen.

Increasing the operating temperature from 200 °C to 300 °C is observed to increase the sensitivity of the sensor and make the response more rapid. Raising the temperature to 400 °C increases the sensitivity more but the sensor seems to be farther from the steady state.

4 Conclusions

In the present work we have investigated structural, chemical, electrical, and gas-sensing properties of an iron oxide thin film grown with ALD at 500 °C. SEM and AFM results indicate that the film has a granular structure and that it has grown mainly on the glass substrate leaving the platinum electrodes uncovered. XRD results show that iron oxide is in the α-Fe_2O_3 (hematite) phase. XPS spectra recorded at an elevated temperature imply that the surface iron is mainly in the Fe^{3+} state and that oxygen has two chemical states: one corresponding to the lattice oxygen and the other to adsorbed oxygen species. Electric conductivity has an activation energy of 0.3–0.5 eV and almost Ohmic I–V dependency. When exposed to O_2 and CO, a typical n-type response was observed.

Acknowledgments

The authors are grateful to Dr. M. Mäkelä (Nanoscale Oy) for the ALD growth of the iron oxide film, Mr. S. Hämäläinen for recording the SEM images and Mr. M. Kainlauri and Mr. T. Hyvämäki for their assistance with the resistance measurement and temperature control equipment. The XRD measurements were performed by the Center for Chemical Analysis, Helsinki University of Technology. The work has been financially supported by the Fortum Foundation and the Academy of Finland.

References

[1] M. J. Madou, S. R. Morrison, Chemical Sensing with Solid State Devices, Academic Press, Inc., 1989.

[2] Y. Nakatani, M. Matsuoka, Jpn. J. Appl. Phys. 21 (1982) L758–L760.

[3] Y. Nakatani, M. Matsuoka, Jpn. J. Appl. Phys. 22 (1983) 233–239.

[4] Y. Nakatani, M. Sakai, M. Matsuoka, Jpn. J. Appl. Phys. 22 (1983) 912–916.

[5] K. Hara, N. Nishida, Sens. Actuators B 20 (1994) 181–186.

[6] A. S. Poghossian, H. V. Abovian, V. M. Aroutiounian, Sens. Actuators B 18 (1994) 155–157.

[7] B. Yan, J. Peng, C. Chai, Thin Solid Films 245 (1994) 225–227.

[8] C. C. Chai, J. Peng, B. P. Yan, Sens. Actuators B 34 (1996) 412–416.

[9] W.-Y. Chung, D.-D. Lee, Thin Solid Films 200 (1991) 329–339.

[10] P. Althainz, L. Schuy, J. Goschnick, H. J. Ache, Thin Solid Films 241 (1994) 366–369.

[11] H.-T. Sun, C. Cantalini, M. Faccio, M. Pelino, Thin Solid Films 269 (1995) 97–101.

[12] X. Q. Liu, S. W. Tao, Y. S. Shen, Sens. Actuators B 40 (1997) 161–165.

[13] S. Wang, W. Wang, W. Wang, Z. Jiao, J. Liu, Y. Qian, Sens. Actuators B 69 (2000) 22–27.

[14] E. Comini, V. Guidi, C. Frigeri, I. Riccó, G. Sberveglieri, Sens. Actuators B 77 (2001) 16–21.

[15] M. Ivanovskaya, D. Kotsikau, G. Faglia, P. Nelli, S. Irikaev, Sens. Actuators B 93 (2003) 422–430.

[16] A. Gurlo, M. Sahm, A. Opera, N. Barsan, U. Weimar, Sens. Actuators B 102 (2004) 291–298.

[17] G. Neri, A. Bonavita, S. Galvagno, Y. X. Li, K. Galatsis, W. Wlodarski, IEEE Sens. J. 3 (2003) 195–198.

[18] G. Neri, A. Bonavita, S. Galvagno, N. Donato, A. Caddemi, Sens. Actuators B 111-112 (2005) 71–77.

[19] Z. Jing, Y. Wang, S. Wu, Sens. Actuators B 113 (2006) 177–181.

[20] T. Suntola, Mater. Sci. Rep. 4 (1989) 261–312.

[21] M. Leskelä, M. Ritala, Thin Solid Films 409 (2002) 138–146.

[22] R. L. Puurunen, J. Appl. Phys. 97 (2005) 121301.

[23] H. Viirola, L. Niinistö, Thin Solid Films 251 (1994) 127–135.

[24] M. de Ridder, P. C. van de Ven, R. G. van Welzenis, H. H. Brongersma, S. Helfensteyn, C. Creemers, P. Van Der Voort, M. Baltes, M. Mathieu, E. F. Vansant, J. Phys. Chem. B 106 (2002) 13146–13153.

[25] B. S. Lim, A. Rahtu, R. G. Gordon, Nat. Mater. 2 (2003) 749.

[26] M. Lie, H. Fjellvåg, A. Kjekshus, Thin Solid Films 488 (2005) 74–81.

[27] M. Utriainen, H. Lattu, H. Viirola, L. Niinistö, R. Resch, G. Friedbacher, Mikrochimica Acta 133 (2000) 119–123.

[28] A. Rosental, A. Tarre, A. Gerst, J. Sundqvist, A. Hårsta, A. Aidla, J. Aarik, V. Sammelselg, T. Uustare, Sens. Actuators B 93 (2003) 552–555.

[29] S. Haukka, E.-L. Lakomaa, O. Jylhä, J. Vilhunen, S. Hornytzkyj, Langmuir 9 (1993) 3497.

[30] A. Kytökivi, E.-L. Lakomaa, A. Root, Langmuir 12 (1996) 4395.

[31] R. L. Puurunen, Chemical Vapor Deposition 11 (2005) 79.

[32] M. Aronniemi, J. Lahtinen, P. Hautojärvi, Surf. Interface Anal. 36 (2004) 1004–1006.

[33] N. Barsan, U. Weimar, J. Electroceram. 7 (2001) 143.

[34] R. F. G. Gardner, F. Sweett, D. W. Tanner, J. Phys. Chem. Solids 24 (1963) 1183.

[35] K. H. Kim, S. H. Lee, J. S. Choi, J. Phys. Chem. Solids 46 (1985) 331.

[36] S. Mochizuki, Phys. Status Solidi A 41 (1977) 591–594.

[37] K. H. Kim, S. H. Lee, J. S. Choi, J. Phys. Chem. Solids 46 (1985) 331–338.

[38] Mineral Powder Diffraction File, Data Book, Card 13-534, JCPDS International Centre for Diffraction Data.

[39] M. Aronniemi, J. Sainio, J. Lahtinen, Surf. Sci. 578 (2005) 108–123.

[40] T. Fujii, F. M. F. de Groot, G. A. Sawatzky, F. C. Voogt, T. Hibma, K. Okada, Phys. Rev. B 59 (1999) 3195–3202.

[41] K. Wandelt, Surf. Sci. Rep. 2 (1982) 1–121.

[42] T. Kawabe, S. Shimomura, T. Karasuda, K. Tabata, E. Suzuki, Y. Yamaguchi, Surf. Sci. 448 (2000) 101–107.

[43] W. Lü, D. Yang, Y. Sun, Y. Guo, S. Xie, H. Li, Appl. Surf. Sci. 147 (1999) 39–43.